

Breaking Abbe's diffraction limit with harmonic deactivation microscopy

Kevin Murzyn^{1†}, Maarten L. S. van der Geest¹, Leo Guery,¹ Zhonghui Nie¹,
Pieter van Essen¹, Stefan Witte^{1,2}, Peter M. Kraus^{1,2*}

¹Advanced Research Center for Nanolithography (ARCNL)
Science Park 106, 1098 XG Amsterdam, Netherlands

²Department of Physics and Astronomy, and LaserLaB, Vrije Universiteit
De Boelelaan 1081, 1081HV Amsterdam, Netherlands

To whom correspondence should be addressed; E-mail: [†] k.murzyn@arcnl.nl, ^{*} p.kraus@arcnl.nl.

Nonlinear optical microscopy provides elegant means for label-free imaging of biological samples and condensed-matter systems. The widespread areas of application could even be increased if resolution was improved, which the famous Abbe diffraction limit currently restrains. Super-resolution techniques can break the diffraction limit but most rely on fluorescent labeling. This makes them incompatible with (sub-)femtosecond temporal resolution and applications that demand the absence of labeling. Here, we introduce harmonic deactivation microscopy (HADES) for breaking the diffraction limit in non-fluorescent samples. By controlling the harmonic generation process on the quantum level with a second donut-shaped pulse, we confine the third harmonic generation to three times below the original focus size of a scanning microscope. We demonstrate that resolution improvement by deactivation is more efficient for higher harmonic orders, and only limited by the max-

imum applicable deactivation-pulse fluence. This provides a route towards sub-100 nm resolution in a regular nonlinear microscope.

Introduction

Far-field optical microscopy has impacted the fields of medicine, biology, and biophysics (1) like hardly any other technique. Microscopy is used as a daily diagnostics tool as well as equipment for cutting-edge scientific advancements. Microscopy benefits from its compactness, ease of use, and the possibility to image 2D as well as 3D objects (2). Third harmonic generation (THG) is used as a label-free microscopy (3) method to study cells (4, 5), photoresists (6) and 2D materials (7). For THG microscopy, an excitation pulse is focused into a material and generates harmonics. The high penetration depth of the near-infrared (NIR) excitation light and the sensitivity to changes in chemical composition are central advantages of THG compared to other optical contrast mechanisms. One challenge preventing an even more widespread application is the limited resolution. The reported resolution of THG microscopes is approximately 1 μm or slightly less (8, 9), which is far from the 200-nm resolution limit commonly stated in a confocal fluorescence microscope (10). This apparent limitation stems from the fact that in typical confocal scanning microscopes, the resolution is proportional to the focus size of the excitation laser of the emission process. This laser is typically in the infrared for harmonic microscopy but in the visible or UV range for fluorescent microscopy. To improve this resolution limit of harmonic microscopy, the emission has to be confined below the diffraction limit. Here we show that the unique optical properties of high-harmonic generation from condensed matter enable sub-diffraction harmonic emission and thus super-resolution microscopy.

High-harmonic generation (HHG) is a laser-driven frequency upconversion process (11, 12), that converts an ultra-short laser pulse into a shorter-wavelength pulse at integer multiples of the fundamental carrier frequency. The discovery of solid-state HHG in 2010 (13) also rejuve-

nated the interest in harmonic generation of lower orders below the bandgap (14) and drove the development of a stringent microscopic theoretical framework (15, 16) that complements the phenomenological framework of perturbative non-linear optics. On the quantum level, HHG is governed by laser-driven electron dynamics and contains signatures of the dynamic electronic structure of the generation medium that can be atoms (17), molecules (18, 19) and solids (13, 20). Inversely, slight variations to these electronic dynamics can have a large impact on the efficiency of HHG (21). In a variety of solids, reversible deactivation of high-harmonics followed the photoexcitation of charge carriers (22–27). Different physical processes are considered to contribute to the deactivation (28, 29) such as state-blocking and ground-state depletion, a decrease in decoherence time (26, 27, 30), and control of electron-hole recollisions in shaped driving waveforms (31). The modulation depth, or contrast, achieved can be close to 100%, demonstrating near-unity-contrast emission control. This intensity modulation is the key enabler of super-resolution HHG microscopy by spatially confining HHG with an optical control pulse.

We took inspiration from the super-resolution techniques in fluorescence microscopy, which can provide resolutions below 10 nm (32). These techniques can be divided into two groups. The first group uses wide-field illumination of the sample and achieves super-resolution through stochastic on-and-off switching of fluorescence combined with localization algorithms (33–36). The second group consists of deterministic methods that rely on targeted modulation or saturation of fluorescence (37–40). Here, we utilize the high modulation depth of HHG (41) for an approach similar to the one used in stimulated emission depletion (STED) microscopy (38) for HHG microscopy. We label this method as harmonic deactivation microscopy (HADES), which relies on an increase in incoherent scattering and disruption of the recombination process through a control beam. In the present manuscript, we focus on THG, but the method will work similarly and with even better resolution for higher harmonic orders. In HADES, we add a donut-shaped deactivation pulse to the infrared driving pulse of HHG. This donut pulse deacti-

vates harmonic emission in the outer parts of the point-spread function (PSF) of the excitation pulse leading to a narrower PSF compared to THG. A similar methodology has been shown for linear microscopy in Silicon (42) and Graphene (43), relying on the plasma dispersion effect and absorption saturation, respectively. The latter hereby was able to achieve a resolution of below 200 nm. For nonlinear microscopy utilizing coherent anti-Raman scattering methods were patented (44) and later shown experimentally (45). Improvements of the resolution of second-harmonic generation microscopy have been shown previously through coherent rescanning (46) and exploiting the nonlinear interaction in a structured illumination microscope (47). A two-fold resolution improvement is achieved through controlling the polarization state over the focus spot (48). In this work we demonstrate a two-dimensional resolution improvement utilizing increased incoherent scattering and recombination during the HHG process.

The combination of ultrafast temporal and nanoscale resolution will be a unique advantage of HADES: Due to the necessity of intramolecular vibrational energy redistribution before stimulated emission in STED, fluorescence super-resolution is inherently incompatible with femtosecond time resolution (49).

While deactivation is a general phenomenon, we chose NbO_2 as a sample in the present manuscript. NbO_2 is a strongly correlated material that undergoes a non-thermal ultrafast insulator-to-metal phase transition (IMT) upon photoexcitation. This phase transition makes strongly correlated materials interesting for a new class of electronic devices such as memristors (50, 51). In recent work HHG was used to probe this transition in NbO_2 and measure its transition time scale to be ~ 100 fs (41). The ability to add super-resolution to resolving IMTs will enable resolving the emergence of different phases with femtosecond temporal and nanometer spatial resolution.

In this letter, we show the time-dependent deactivation behavior of THG in NbO_2 and how it's governed by the fluence of the deactivation beam. These results are used to predict a change in the PSF of the third harmonic in HADES. We then change in our experiment the deactivation

beam profile to a donut shape and confirm the narrower PSF. Conclusively, we improve the resolution of a scanning THG microscope by implementing HADES.

Results

Deactivation of third harmonic generation. The concept of the experiment is illustrated in Fig. 1. In regular harmonic microscopy, a NIR excitation laser generates harmonic multiples of its fundamental frequency. For a Gaussian intensity distribution I_{NIR} of the fundamental NIR excitation laser in focus (Fig. 1a), the intensity distribution of the third harmonic will also be Gaussian (Fig. 1c). The spatial emission intensity distribution, called point-spread function (PSF), of HHG is narrower than the excitation pulse PSF and scales in the perturbative regime with $I_{HHG} \propto I_{NIR}^n$, where n is the power law exponent of the process which is approximately three for THG. In this work, we further deactivate HHG spatially by adding a pulse that is donut-shaped in focus to HHG (Fig. 1b). This donut-shaped pulse is achieved by imparting an orbital angular momentum onto the deactivation pulse by means of a spiral phase plate inserted in the far-field pulse profile. This concept allows deactivating HHG to a narrower emission peak below the diffraction limit (Fig. 1d) since HHG is deactivated in regions of non-zero intensity of the donut-shaped deactivation pulse. By narrowing the spot size below the diffraction limit, we can implement a super-resolution label-free scanning microscope.

We use a modified Mach-Zehnder interferometer to realize these experiments (Fig. S1). The fundamental HHG driving pulse is centered at a wavelength of 1830 nm, while the donut pulse is centered at 400 nm. Both pulses are linearly and parallel polarized. Detailed descriptions of all experiments can be found in the materials and methods section.

We first characterize the deactivation behavior by measuring the spectra of the emitted harmonics. We vary the delay between the pulses (Fig. 2a) as well as the intensity of the deactivation pulse (Fig. 2b). The spectral shape of the third harmonic (inset Fig. 2b) stays identical for all

fluences. However, with increasing modulation fluence the amplitude and the integrated signal reduce. We normalize the integrated signal to its deactivation, i.e. a normalized deactivation of one means full deactivation of HHG so that there is no measurable signal, while zero means the signal is unchanged. When the driving pulse arrives before the deactivation pulse no change in the THG can be observed. This is followed by a sharp increase in the maximum deactivation when both pulses arrive simultaneously. At increasing time delays the signal recovers with a fast and slow exponential component, consistent with the results in (41).

The deactivation becomes stronger the higher the deactivation-pulse fluence. However, no dependence on the relative polarization angle could be observed during the experiments. At the highest deactivation-pulse fluence of 24 mJ/cm^2 , the integrated signal amounts to 2% of the reference at the temporal overlap of the two pulses. From this fluence dependence of the normalized deactivation, we determine a saturation fluence Φ_{sat} , defined as the fluence at half deactivation, of 2.5 mJ/cm^2 , while the intensity modulation depth is 98%. Comparing these results to deactivation curves for the fifth harmonic (grey curve Fig. 2b) shows that higher-order harmonics have a lower saturation fluence of 1.8 mJ/cm^2 .

While other STED-like techniques have been proposed and implemented in the past (45, 48), our approach - HADES - sets itself apart, both in its physical mechanism and its prospect for broad applicability. These intertwined features - broad applicability through a new mechanism - rest on how solid HHG can be deactivated by a modulation pulse, which is first and foremost a property of the HHG process on the quantum level as well as the driving field, but not of the material. The mechanistic understanding of solid harmonic generation has been rejuvenated in recent years (20) and extended beyond the phenomenological perturbative nonlinear picture. Solid HHG is understood to originate from two contributions following multiphoton excitation across the band gap. HHG is emitted from an intraband carrier current, as well as an interband polarization due to coherent electron-hole pairs. This interband polarization can

be thought to originate from an electron-hole recollision. If a second modulation pulse is applied to control the HHG process, several phenomena occur as detailed in our recent perspective article on the topic (28) and briefly reviewed here: First, two-color waveforms strongly modulate HHG (52, 53), and the waveform of two overlapping electric fields (i.e. at a time delay of zero) with incommensurate frequencies can decrease the overall intensity within a harmonic order (54). Second, right after excitation and for later times (i.e. for delays of and larger than zero) the coherent electron-hole pairs excited from the HHG driving pulse dephase faster due to the excited carrier population from the first pulse. In general, an excited carrier population promotes both accelerated carrier-carrier and carrier-phonon scattering, thus leading to a rapid loss of electron-hole coherence (23, 27). It is this electron-hole coherence which is necessary for efficient HHG, so an increased dephasing causes an amplitude reduction and thus deactivation of HHG. In the specific case of NbO_2 , photo-excitation triggers an ultrafast phase transition on a time scale of 100 fs (41) into a metallic phase, where electron scattering is generally larger and thus the effect of HHG suppression through loss of electron-hole coherence is further enhanced. Scattering and the associated dephasing-time reduction act as amplitude suppression (41) window onto the time-domain emission of HHG, thus reducing the overall emission intensity. Both effects - waveform modulation and increased electron dephasing are contributing to deactivation in our experiment. This is evidenced by the observation of the highest levels of HHG deactivation at time zero for all pump fluences, which can thus be partially attributed to waveform modulation. Furthermore, the persisting high level of HHG deactivation after time zero can be attributed to increased scattering due to excited electrons and also an insulator-to-metal phase transition at higher pump fluences. At a time delay of zero, where the experiments described in this article are performed, both effects can thus play a role. Critically, none of these processes rely on resonant transitions in the material itself as the harmonic deactivation has been shown also for below bandgap pumping (28, 31, 55).

Point-spread function reduction. We first estimate the expected resolution improvement of HADES for a one-dimensional model. We combine the fluence-dependent deactivation with the spatial distribution of the intensity of the donut pulse and multiply this with an initial Gaussian distribution of the emitted harmonics. Assuming a maximum fluence of 25 mJ/cm^2 , this one-dimensional model results in a PSF reduction by a factor of three (Fig. S2). This requires that the donut-shaped pulse has a constant azimuthal fluence distribution and that the maximum of the donut coincides with the FWHM of the THG, since a larger donut pulse lessens the effective applied fluence and a smaller donut pulse produces side wings which lead to smearing. In the above model, we chose to use a \cos^2 function for modeling the donut-shaped deactivation profile as previously done in (56) for STED microscopy. We, therefore, modify the resulting formula to be adapted for our measurements as (56):

$$d = \frac{\lambda_0}{2\text{NA}\sqrt{n}} \frac{1}{\sqrt{1+\zeta}}. \quad (1)$$

The first term containing the wavelength of the fundamental excitation laser λ_0 , nonlinear order n (three or five for detection of the third or fifth harmonic, respectively, in the perturbative regime) and numerical aperture NA, is the diffraction limit after Abbe modified for harmonic microscopy. The second term gives the resolution improvement based on the saturation level $\zeta = \Phi_{\text{HADES}}^{\text{peak}}/\Phi_{\text{sat}}$. If we assume a peak fluence $\Phi_{\text{HADES}}^{\text{peak}}$ of 24 mJ/cm^2 and the measured saturation fluence for the third harmonic the resolution improves by a factor of 3.3, which is close to our one-dimensional model. For fifth harmonic generation, we calculate a resolution improvement of 3.8. This shows pathways to improve the resolution even further by decreasing the saturation fluence, e.g. via optimizing the deactivation scheme or by using higher-order harmonics that deactivate at lower fluences.

We now demonstrate this all-optical control and shrinkage of the PSF. A lens with a focal length of 25 cm generates the third harmonic in the sample (Fig. 3a). A home-built bright-field micro-

scope images the PSF in transmission. We calculate the diffraction limit of the lens that focuses the driving pulses as $40.7 \pm 1.2 \text{ } \mu\text{m}$, which is the first term in eq. (1). The unchanged third harmonic PSF (Fig. 3b) has an FWHM of $40 \pm 1.5 \text{ } \mu\text{m}$, which is in agreement with the theoretical diffraction limit. When the donut pulse (inset figure 3c) deactivates the third harmonic emission the area that emits light is drastically reduced to an FWHM of $14 \pm 0.6 \text{ } \mu\text{m}$, while the peak intensity stays similar. This yields a reduction of factor 2.9 ± 0.15 , which matches the prediction of the one-dimensional model. Based on the experimental data, we calculated a two-dimensional model, which also shows a PSF reduction although this is limited by the diffraction from the uneven sample surface (Fig S3). The emission spot produced via HADES is therefore roughly three times smaller than Abbe’s diffraction limit in eq. (1). This paves the way towards a feasible approach for label-free super-resolution scanning microscopy through HADES, which we demonstrate in the next section in a proof-of-principle experiment.

Microscopic imaging. For rapid sampling, the fundamental pulse of 800 nm was used for deactivation since a similar deactivation behavior to 400 nm was observed. We used a lens with a focal length of 5 cm as the focusing objective, which also captured the back-reflected THG for imaging (Fig. 4a). In the detection pathway, a series of bandpass filters (BP) select a specific harmonic order. A tube lens then focuses the filtered light onto an avalanche photodiode (APD). The APD measures signal with low average powers on a shot-to-shot basis, enabling rapid scanning of the sample. A boxcar integrator filters out noise outside the 2% duty cycle. Figures 4b) and c) show the recorded pictures for THG microscopy and HADES, respectively. These pictures depict the transition from an area with laser-induced damage to an undamaged sample area. The large dark area (area with no signal) has no thin film left, while the area emitting a lot of signal (red area) still has thin film. We analyze the origin of the sharp intensity features in the discussion. In comparison, the HADES picture visualizes smaller details compared to THG

microscopy. The super-resolution becomes visible when convolving the HADES image with a Gaussian. This fully reproduces the THG microscopy image (Fig. S4), which demonstrates the resolution improvement by HADES. The two profiles (Fig. 4d) exemplify this resolution improvement further. Along the dotted line in the THG microscope, a single peak is imaged while by using HADES two peaks become distinguishable. These two peaks are separated by $9.7\text{ }\mu\text{m}$. The dotted line depicts a single peak at the very edge of the thin film. With THG microscopy the FWHM of this emitter is $15.6\text{ }\mu\text{m}$, while, with HADES the FWHM reduces to $7.1\text{ }\mu\text{m}$. These examples can be quantified further by the use of a Fourier ring correlation (FRC) (57) analysis. First, a mask was applied to the Fourier transform of the images to suppress scanning artifacts. The FRC shows a higher correlation at larger spatial frequencies for HADES (Fig. S5). We choose the $1/7$ -threshold (58), as it is a common threshold for resolution estimation in 2D. This threshold yields a resolution limit of $8.6\text{ }\mu\text{m}$ and $5.5\text{ }\mu\text{m}$ for THG and HADES, respectively. We show, therefore, that the resolution improves in two dimensions at the same time.

Discussion

We now turn to discussing signal formation in HADES. The image shows an area of the NbO_2 thin film that was thermally damaged before the HADES experiments. In bright-field microscopy, the dark area is visible as well, indicating that material was ablated (Fig. S6a) when damage occurred. The bright spot (dashed profile in Fig. 4) is located at a pointy tip of the thin film to pure substrate transition seen in dark-field microscopy (Fig. S6b). A combination of multiple effects can be the reason for the enhancement THG signal enhancement at this bright spot. First, the third-order susceptibility of the sample can be changed locally, since the NbO_2 thin film generates harmonics more efficiently than the pure substrate. Second, near-field confinements of the electric field of the fundamental in subwavelength nanostructures can enhance the HHG efficiency (59). Indeed, the presence of such sub-wavelength nanostructures becomes

visible under a scanning electron microscope (Fig. S7). During experimenting, we generally observed an enhancement of the signal when scanning over an edge in the sample, indicating near-field enhancement of the fundamental field, which boosts the efficiency of HHG locally. Our current experimental procedure was challenged by the available low repetition rate (2 kHz) / high-pulse energy (3.5 mJ) laser system. The high pulse energies required a strong attenuation of both the modulation and excitation pulse by effective optical densities up to 5, which made detectable signals weak due to the 2-kHz repetition rate. These requirements made optimization more challenging especially for shorter focal lengths lenses. Furthermore, scanning microscopy as shown in Fig. 4 will benefit from either high-speed scanning stages or ideally a galvo-mirror system that scans the position of the focus through the objective, neither of which was available for the current experiment. Implementing both - higher repetition rate lasers and high-speed scanning will make taking microscopy images in seconds possible. This will also allow focusing the HHG driving pulses with high-NA objectives instead of lenses (Fig. 4). Since we have demonstrated the mechanism for breaking the diffraction limit in harmonic microscopy in this manuscript, we now understand that we can quantitatively predict the resolution improvement by means of Eq. 1 and the harmonic deactivation curve (Fig. 2b).

The ideas presented can be extended to tighter focusing conditions emitting higher harmonics. The in-depth analysis of the deactivation process measured here and by (41) delivers a three-times resolution improvement of THG microscopy and a 3.8-times resolution improvement for a fifth harmonic generation microscope. Considering a near-infrared excitation at 1800 nm and a high NA objective of 1.35, the expected resolutions for the specific set of wavelengths, polarizations, and material (NbO_2) chosen here are 120 nm for THG and 80 nm for the fifth harmonic generation. These estimations are made based on eq. (1) and the experimental findings done in this paper and by (41), which yields a saturation fluence of 1.8 mJ/cm^2 for the fifth harmonic. The maximum applicable fluence was hereby always low enough to not damage the

sample itself, meaning that laser-induced damage ultimately limits this technique. Deepening the understanding of the deactivation process for harmonic generation in materials will lead to an even better resolution by either reducing the saturation fluence, i.e. finding ways to deactivate HHG more efficiently, or by extending the highest applicable peak fluence. This principle is ultimately not limited to the deactivation of HHG by photoexcited carriers, which limits the maximum applicable fluence due to photo-induced damage. Other deactivation methods are also suited for this, i.e. control of the electron-hole recombination with a combination of below band-gap driving wavelengths might also be a suitable pathway (31). Ultimately, resolution in HADES is only limited by the real-space excursion of electrons and holes by the driving laser pulse. This excursion underlies the microscopic currents that radiate HHG, and corresponds to a real-space displacement on the single-digit nanometer scale, the exact value of which depends on electronic structure and laser parameters. As a hypothetical deactivation below this limit would truncate HHG even from the inner region without a deactivation pulse, this excursion length scale sets the ultimate resolution limit for HADES. Furthermore, other optical nonlinearities such as coherent anti-Stokes Raman scattering (60), stimulated Raman scattering (61), or sum frequency generation (62) can be used to achieve super-resolution with similar concepts. However, the extreme nonlinearity of HHG creates a maximum sensitivity to control pulses. This likely makes HHG and related high-order frequency mixing processes the ideal candidates for resolution improvement by deactivation in particular, and optical emission control and optical switching in general. The wide range of solid-state materials, which have shown harmonic deactivation (28), make HADES an interesting candidate for metrology on dielectric and semi-conducting materials, as well as, an important research tool for material science. Purley field effect-driven harmonic deactivation allows even application in biological samples.

Materials and Methods

Materials

The sample investigated in this study is the polycrystalline thin film NbO₂, which was grown on a c-plane sapphire substrate through reactive bias target ion pulse deposition (RBTIBD), and the more information of the material synthesis are available in previous literature (41, 63). The Raman spectrum and X-ray diffraction 2θ scan are both utilized to confirm the high quality and the bct lattice structure of our sample. Any other oxide components (NbO or Nb₂O₅) have not been found. The thickness of our sample is ~ 115 nm, measured by X-ray reflectivity, and its surface roughness is less than 1 nm. Moreover, the sapphire substrates are double-side polished, ensuring the possibility of transmission measurements.

Methods

Laser system and experimental setup. A Ti:Sapphire laser amplifier (Solstice, Spectra-Physics) produces a laser pulse at a central wavelength of 790 nm and with a pulse duration below 72 fs. The repetition rate is set to 2 kHz while the average output power is 7 W. A pulse splitter (BS) sends the laser light into each of the arms. In the excitation arm, the light pumps an optical parametric amplifier (OPA, Topas prime), which emits NIR light centered at 1800 nm. The idler of the parametric process was used to generate the third harmonic since only the idler can reach the desired wavelength. In the modulation arm, the delay of the 800 nm pulse can be adjusted by a mechanical delay stage. This is called the modulating arm. Afterward, a spiral phase plate (PP) converts the intensity profile into a donut shape. Optionally, a second harmonic generation BBO can be introduced after the spiral phase plate to change the central wavelength to 400 nm. Variable attenuators control the average power in each arm independently, while telescopes set the pulse size. A dichroic mirror (DM) combines the two pulses. After this, an objective lens (Obj) focuses this pulse bundle onto the sample (S). The modulation arm uses a

combination of a half-wave plate and polarizer for a first attenuation, a second attenuation is achieved by a variable neutral density filter wheel. The excitation arm is attenuated by a series of neutral density filters. A schematic of the experiment can be found in the supplementary information (Fig. S1).

Deactivation measurements. For the deactivation measurements, we removed the spiral phase plate from the modulation arm. A telescope focuses the modulation pulse so that it has an FWHM of 200 μm while the excitation NIR pulse has an FWHM of 40 μm . A tube lens focuses the back-reflected harmonics into a fiber spectrometer (Ocean Insight, QE Pro), that resolves the spectral composition of the harmonics.

PSF imaging. A microscope objective (Mitutoyo Plan Apo NIR B) collimates the light from the sample with a magnification of 20x and an NA of 0.4. Subsequently, a tube lens with a focal length of 20 cm images them onto a camera. A pair of Bandpass filters blocked the donut pulse for PSF imaging. They have a central wavelength of 600 nm and a FWHM of 40 nm. The donut pulse was attenuated by an ND filter with an OD of 4.0 to avoid permanent damage. We evaluated the FWHM of the PSF by binarizing the images at a relative intensity of 0.5. Then an ellipse was fitted to the mask created that way. The FWHM represents the average radius of the fitted ellipse.

Microscopy pictures. For the microscopy images both arms had to be attenuated by an effective optical density of 5. Otherwise, the high pulse energy of the laser could damage the thin-film surface. An 800 nm pulse deactivated the third harmonic response. To make scanning images we used a lens with a focal length of 5 cm and detected the reflected third harmonic emission. A silicon-based analog APD (Thorlabs) produces the signal out of the third harmonic generation. A preamplifier amplified the voltage output of the APD before the pulsed signal was

integrated using a boxcar integrator. The Voltage output was then digitized by a data acquisition card. A piezo stage moved the sample through the focused pulse from spot to spot.

The images have a pixel size of 1 μm in both directions and are 51 x 51 pixels large. The images were scanned line by line. For the THG microscopy at each pixel 25 laser pulses were measured and each line was repeated 3 times, while for HADES each line was repeated 12 times with 25 laser pulses per pixel to ensure a similar count of photons for each pixel. The microscopy pictures displayed are the averaged values of each measurement, normalized to the maximum and minimum values. For the profile generation, the images were smoothed using a median filter with a pixel radius of 1.5. The profiles were generated with the profile plotter of ImageJ. The profiles were again normalized and interpolated by a spline algorithm for measurements of the FWHM of the features and measurements of the peak separation.

Acknowledgments

Acknowledgments: We thank Christoph Morscher for help with dark-field images. We thank Antonios Pelekanidis for helping with the step-phase plates. We thank Matthijs Velsink for help with the APD. We thank the AMOLF support department for providing and helping with the measurement software and hardware.

Funding: This work was conducted at the Advanced Research Center for Nanolithography, a public-private partnership between the University of Amsterdam (UvA), Vrije Universiteit Amsterdam (VU), Rijksuniversiteit Groningen (RUG), the Netherlands Organization for Scientific Research (NWO), and the semiconductor equipment manufacturer ASML and was (partly) financed by ‘Toeslag voor Topconsortia voor Kennis en Innovatie (TKI)’ from the Dutch Ministry of Economic Affairs and Climate Policy. This manuscript is part of a project that has received funding from the European Research Council (ERC) under the European Union’s Horizon Eu-

rope research and innovation programme (grant agreement no. 101041819, ERC Starting Grant ANACONDA). Z.N., L.G., S.W. and P.M.K. acknowledge support from the Open Technology Programme (OTP) by NWO, grant no. 18703. The project is also part of the VIDI research programme HIMALAYA with project number VI.Vidi.223.133 financed by NWO.

Author contribution: K.M., L.G., S.W., and P.M.K. envisioned and conceptualized the experiments. K.M. and P.M.K. carried out a preliminary experiment, and K.M., M.L.S.G., and P.E. carried out the main experiments. K.M. and Z.N. analyzed the data. L.G. and Z.N. provided and characterized the sample. P.M.K. supervised the work. K.M. and P.M.K. wrote a first version of the manuscript that was finalized by all authors.

Competing interest: The authors declare that they have no competing interests.

Data availability: All data needed to evaluate the conclusions in the paper are present in the paper and/or the Supplementary Materials.

References

1. S. Weisenburger, V. Sandoghdar, Light microscopy: an ongoing contemporary revolution. *Contemporary Physics* **56**, 123-143 (2015).
2. J. Mertz, *Introduction to optical microscopy* (Cambridge University Press, 2019).
3. M. D. Duncan, J. Reintjes, T. J. Manuccia, Scanning coherent anti-stokes raman microscope. *Optics Letters* **7**, 350–352 (1982).
4. D. Débarre, W. Supatto, A. M. Pena, A. Fabre, T. Tordjmann, L. Combettes, M. C. Schanne-Klein, E. Beaupaire, Imaging lipid bodies in cells and tissues using third-harmonic generation microscopy. *Nature Methods* **3**, 47–53 (2006).

5. S. Witte, A. Negrean, J. C. Lodder, C. P. De Kock, G. T. Silva, H. D. Mansvelder, M. L. Groot, Label-free live brain imaging and targeted patching with third-harmonic generation microscopy. *Proceedings of the National Academy of Sciences of the United States of America* **108**, 5970–5975 (2011).
6. L. Kallioniemi, S. Annurakshita, G. Bautista, Third-harmonic generation microscopy of undeveloped photopolymerized structures. *OSA Continuum* **3**, 2961 (2020).
7. L. Zhou, H. Fu, T. Lv, C. Wang, H. Gao, D. Li, L. Deng, W. Xiong, Nonlinear optical characterization of 2d materials. *Nanomaterials* **10**, 1–38 (2020).
8. M. Yildirim, N. Durr, A. Ben-Yakar, Tripling the maximum imaging depth with third-harmonic generation microscopy. *Journal of Biomedical Optics* **20**, 096013 (2015).
9. Y. Murakami, M. Masaki, S. Miyazaki, R. Oketani, Y. Hayashi, M. Yanagisawa, S. Honjoh, H. Kano, Spectroscopic second and third harmonic generation microscopy using a femtosecond laser source in the third near-infrared (NIR-III) optical window. *Biomedical Optics Express* **13**, 694 (2022).
10. L. Shao, P. Kner, E. H. Rego, M. G. Gustafsson, Super-resolution 3d microscopy of live whole cells using structured illumination. *Nature methods* **8**, 1044–1046 (2011).
11. A. McPherson, G. Gibson, H. Jara, U. Johann, T. S. Luk, I. McIntyre, K. Boyer, C. K. Rhodes, Studies of multiphoton production of vacuum-ultraviolet radiation in the rare gases. *JOSA B* **4**, 595–601 (1987).
12. M. Ferray, A. L’Huillier, X. F. Li, L. A. Lompre, G. Mainfray, C. Manus, Multiple-harmonic conversion of 1064 nm radiation in rare gases. *Journal of Physics B: Atomic, Molecular and Optical Physics* **21**, L31 (1988).

13. S. Ghimire, A. D. Dichiaro, E. Sistrunk, P. Agostini, L. F. Dimauro, D. A. Reis, Observation of high-order harmonic generation in a bulk crystal. *Nature Physics* **7**, 138–141 (2011).
14. P. Jürgens, B. Liewehr, B. Kruse, C. Peltz, D. Engel, A. Husakou, T. Witting, M. Ivanov, M. Vrakking, T. Fennel, *et al.*, Origin of strong-field-induced low-order harmonic generation in amorphous quartz. *Nature Physics* **16**, 1035–1039 (2020).
15. D. Golde, T. Meier, S. W. Koch, High harmonics generated in semiconductor nanostructures by the coupled dynamics of optical inter- and intraband excitations. *Physical Review B* **77**, 075330 (2008).
16. O. Schubert, M. Hohenleutner, F. Langer, B. Urbanek, C. Lange, U. Huttner, D. Golde, T. Meier, M. Kira, S. W. Koch, *et al.*, Sub-cycle control of terahertz high-harmonic generation by dynamical Bloch oscillations. *Nature Photonics* **8**, 119–123 (2014).
17. A. Shiner, B. Schmidt, C. Trallero-Herrero, H. J. Wörner, S. Patchkovskii, P. B. Corkum, J. Kieffer, F. Légaré, D. Villeneuve, Probing collective multi-electron dynamics in xenon with high-harmonic spectroscopy. *Nature Physics* **7**, 464–467 (2011).
18. O. Smirnova, Y. Mairesse, S. Patchkovskii, N. Dudovich, D. Villeneuve, P. Corkum, M. Y. Ivanov, High harmonic interferometry of multi-electron dynamics in molecules. *Nature* **460**, 972–977 (2009).
19. P. M. Kraus, B. Mignolet, D. Baykusheva, A. Rupenyan, L. Horný, E. F. Penka, G. Grassi, O. I. Tolstikhin, J. Schneider, F. Jensen, *et al.*, Measurement and laser control of attosecond charge migration in ionized iodoacetylene. *Science* **350**, 790–795 (2015).
20. S. Ghimire, D. A. Reis, High-harmonic generation from solids. *Nature Physics* **15**, 10–16 (2019).

21. P. M. Kraus, S. B. Zhang, A. Gijsbertsen, R. R. Lucchese, N. Rohringer, H. J. Wörner, High-harmonic probing of electronic coherence in dynamically aligned molecules. *Physical Review Letters* **111**, 1–5 (2013).
22. Z. Wang, H. Park, Y. H. Lai, J. Xu, C. I. Blaga, F. Yang, P. Agostini, L. F. DiMauro, The roles of photo-carrier doping and driving wavelength in high harmonic generation from a semiconductor. *Nature Communications* **8**, 1–7 (2017).
23. C. Heide, Y. Kobayashi, A. C. Johnson, F. Liu, T. F. Heinz, D. A. Reis, S. Ghimire, Probing electron-hole coherence in strongly driven 2D materials using high-harmonic generation. *Optica* **9**, 512 (2022).
24. Y. Wang, F. Iyikanat, X. Bai, X. Hu, S. Das, Y. Dai, Y. Zhang, L. Du, S. Li, H. Lipsanen, F. J. García De Abajo, Z. Sun, Optical Control of High-Harmonic Generation at the Atomic Thickness. *Nano Letters* **22**, 8455–8462 (2022).
25. M. R. Bionta, E. Haddad, A. Leblanc, V. Gruson, P. Lassonde, H. Ibrahim, J. Chaillou, N. Émond, M. R. Otto, Á. Jiménez-Galán, R. E. Silva, M. Ivanov, B. J. Siwick, M. Chaker, F. Légaré, Tracking ultrafast solid-state dynamics using high harmonic spectroscopy. *Physical Review Research* **3**, 1–12 (2021).
26. Y. Cheng, H. Hong, H. Zhao, C. Wu, Y. Pan, C. Liu, Y. Zuo, Z. Zhang, J. Xie, J. Wang, D. Yu, Y. Ye, S. Meng, K. Liu, Ultrafast Optical Modulation of Harmonic Generation in Two-Dimensional Materials. *Nano Letters* (2020).
27. M. L. S. van der Geest, J. J. de Boer, K. Murzyn, P. Jürgens, B. Ehrler, P. M. Kraus, Transient high-harmonic spectroscopy in an inorganic–organic lead halide perovskite. *The Journal of Physical Chemistry Letters* **14**, 10810–10818 (2023). PMID: 38015825.

28. P. J. van Essen, Z. Nie, B. de Keijzer, P. M. Kraus, Towards complete all-optical emission control of high-harmonic generation from solids (2024).
29. B. de Keijzer, P. J. van Essen, P. M. Kraus, Effect of photoexcitation on high-harmonic generation in semiconductors. *Journal of the Optical Society of America B* **41**, 1754–1763 (2024).
30. G. G. Brown, Á. Jiménez-Galán, R. E. F. Silva, M. Ivanov, A Real-Space Perspective on Dephasing in Solid-State High Harmonic Generation. *arXiv* pp. 1–6 (2022).
31. Y. Wang, Y. Liu, P. Jiang, Y. Gao, H. Yang, L. Y. Peng, Q. Gong, C. Wu, Optical switch of electron-hole and electron-electron collisions in semiconductors. *Physical Review B* **107**, 1–5 (2023).
32. M. Weber, H. von der Emde, M. Leutenegger, P. Gunkel, S. Sambandan, T. A. Khan, J. Keller-Findeisen, V. C. Cordes, S. W. Hell, MINSTED nanoscopy enters the Ångström localization range. *Nature Biotechnology* **41** (2023).
33. E. Betzig, Proposed method for molecular optical imaging. *Opt. Lett.* **20**, 237–239 (1995).
34. E. Betzig, G. H. Patterson, R. Sougrat, O. W. Lindwasser, S. Olenych, J. S. Bonifacino, M. W. Davidson, J. Lippincott-Schwartz, H. F. Hess, Imaging intracellular fluorescent proteins at nanometer resolution. *Science* **313**, 1642–1645 (2006).
35. M. J. Rust, M. Bates, X. Zhuang, Sub-diffraction-limit imaging by stochastic optical reconstruction microscopy (STORM). *Nature Methods* **3**, 793–795 (2006).
36. A. Sharonov, R. M. Hochstrasser, Wide-field subdiffraction imaging by accumulated binding of diffusing probes. *Proceedings of the National Academy of Sciences of the United States of America* **103**, 18911–18916 (2006).

37. S. W. Hell, J. Wichmann, Breaking the diffraction resolution limit by stimulated emission: stimulated-emission-depletion fluorescence microscopy. *Optics Letters* **19**, 780 (1994).
38. T. A. Klar, S. Jakobs, M. Dyba, A. Egner, S. W. Hell, Fluorescence microscopy with diffraction resolution barrier broken by stimulated emission. *Proceedings of the National Academy of Sciences of the United States of America* **97**, 8206–8210 (2000).
39. S. W. Hell, M. Kroug, Ground-state-depletion fluorescence microscopy: A concept for breaking the diffraction resolution limit. *Applied Physics B* **60**, 495–497 (1995).
40. M. G. Gustafsson, Nonlinear structured-illumination microscopy: Wide-field fluorescence imaging with theoretically unlimited resolution. *Proceedings of the National Academy of Sciences of the United States of America* **102**, 13081–13086 (2005).
41. Z. Nie, L. Guery, E. B. Molinero, P. Juergens, T. J. van den Hooven, Y. Wang, A. Jimenez Galan, P. C. M. Planken, R. E. F. Silva, P. M. Kraus, Following the nonthermal phase transition in niobium dioxide by time-resolved harmonic spectroscopy. *Phys. Rev. Lett.* **131**, 243201 (2023).
42. H. Pinhas, O. Wagner, Y. Danan, M. Danino, Z. Zalevsky, M. Sinvani, Plasma dispersion effect based super-resolved imaging in silicon. *Optics Express* **26**, 25370 (2018).
43. P. Wang, M. N. Slipchenko, J. Mitchell, C. Yang, E. O. Potma, X. Xu, J. X. Cheng, Far-field imaging of non-fluorescent species with subdiffraction resolution. *Nature Photonics* **7**, 449–453 (2013).
44. H. Kanou, Y. Iketaki, Super-resolution microscope (Japan Patent JP2018120006A, Jan. 2017).

45. L. Gong, W. Zheng, Y. Ma, Z. Huang, Higher-order coherent anti-Stokes Raman scattering microscopy realizes label-free super-resolution vibrational imaging. *Nature Photonics* **14**, 115–122 (2020).
46. D. Raanan, M. S. Song, W. A. Tisdale, D. Oron, Super-resolved second harmonic generation imaging by coherent image scanning microscopy. *Applied Physics Letters* **120** (2022).
47. J. J. Field, K. A. Wernsing, S. R. Domingue, A. M. Motz, K. F. DeLuca, D. H. Levi, J. G. DeLuc, M. D. Young, J. A. Squier, R. A. Bartels, Superresolved multiphoton microscopy with spatial frequency-modulated imaging. *Proceedings of the National Academy of Sciences of the United States of America* **113**, 6605–6610 (2016).
48. O. Masihzadeh, P. Schlup, R. A. Bartels, Enhanced spatial resolution in third-harmonic microscopy through polarization switching. *Optics Letters* **34**, 1240 (2009).
49. S. B. Penwell, L. D. Ginsberg, R. Noriega, N. S. Ginsberg, Resolving ultrafast exciton migration in organic solids at the nanoscale. *Nature Materials* **16**, 1136–1141 (2017).
50. Z. Yang, C. Ko, S. Ramanathan, Oxide electronics utilizing ultrafast metal-insulator transitions. *Annual Review of Materials Research* **41**, 337–367 (2011).
51. S. Kumar, R. S. Williams, Z. Wang, Third-order nanocircuit elements for neuromorphic engineering. *Nature* **585**, 518–523 (2020).
52. S. R. Abbing, F. Campi, F. S. Sajjadian, N. Lin, P. Smorenburg, P. M. Kraus, Divergence control of high-harmonic generation. *Physical Review Applied* **13**, 054029 (2020).
53. S. D. Roscam Abbing, F. Campi, A. Zeltsi, P. Smorenburg, P. M. Kraus, Divergence and efficiency optimization in polarization-controlled two-color high-harmonic generation. *Scientific Reports* **11**, 24253 (2021).

54. M. Negro, C. Vozzi, K. Kovacs, C. Altucci, R. Velotta, F. Frassetto, L. Poletto, P. Villoresi, S. de Silvestri, V. Tosa, S. Stagira, Gating of high-order harmonics generated by incommensurate two-color mid-IR laser pulses. *Laser Physics Letters* **8**, 875–879 (2011).
55. S. Xu, H. Zhang, J. Yu, Y. Han, Z. Wang, J. Hu, Ultrafast modulation of a high harmonic generation in a bulk ZnO single crystal. *Optics Express* **30**, 41350 (2022).
56. V. Westphal, S. W. Hell, Nanoscale resolution in the focal plane of an optical microscope. *Physical Review Letters* **94**, 1–4 (2005).
57. S. Koho, G. Tortarolo, M. Castello, T. Deguchi, A. Diaspro, G. Vicidomini, Fourier ring correlation simplifies image restoration in fluorescence microscopy. *Nature Communications* **10** (2019).
58. M. Van Heel, M. Schatz, Fourier shell correlation threshold criteria. *Journal of Structural Biology* **151**, 250–262 (2005).
59. S. D. Roscam Abbing, R. Kolkowski, Z. Y. Zhang, F. Campi, L. Lötgering, A. F. Koenderink, P. M. Kraus, Extreme-Ultraviolet Shaping and Imaging by High-Harmonic Generation from Nanostructured Silica. *Physical Review Letters* **128**, 223902 (2022).
60. W. P. Beeker, C. J. Lee, K. J. Boller, P. Groß, C. Cleff, C. Fallnich, H. L. Offerhaus, J. L. Herek, A theoretical investigation of super-resolution CARS imaging via coherent and incoherent saturation of transitions. *Journal of Raman Spectroscopy* **42**, 1854–1858 (2011).
61. S. Zhang, J. Shi, H. Zhang, T. Jia, Z. Wang, Z. Sun, Precise control of state-selective excitation in stimulated Raman scattering. *Physical Review A - Atomic, Molecular, and Optical Physics* **82**, 4–7 (2010).

62. K. Sekiguchi, S. Yamaguchi, T. Tahara, Femtosecond time-resolved electronic sum-frequency generation spectroscopy: A new method to investigate ultrafast dynamics at liquid interfaces. *Journal of Chemical Physics* **128** (2008).
63. Y. Wang, R. B. Comes, S. Kittiwatanakul, S. A. Wolf, J. Lu, Epitaxial niobium dioxide thin films by reactive-biased target ion beam deposition. *Journal of Vacuum Science & Technology A* **33** (2015).

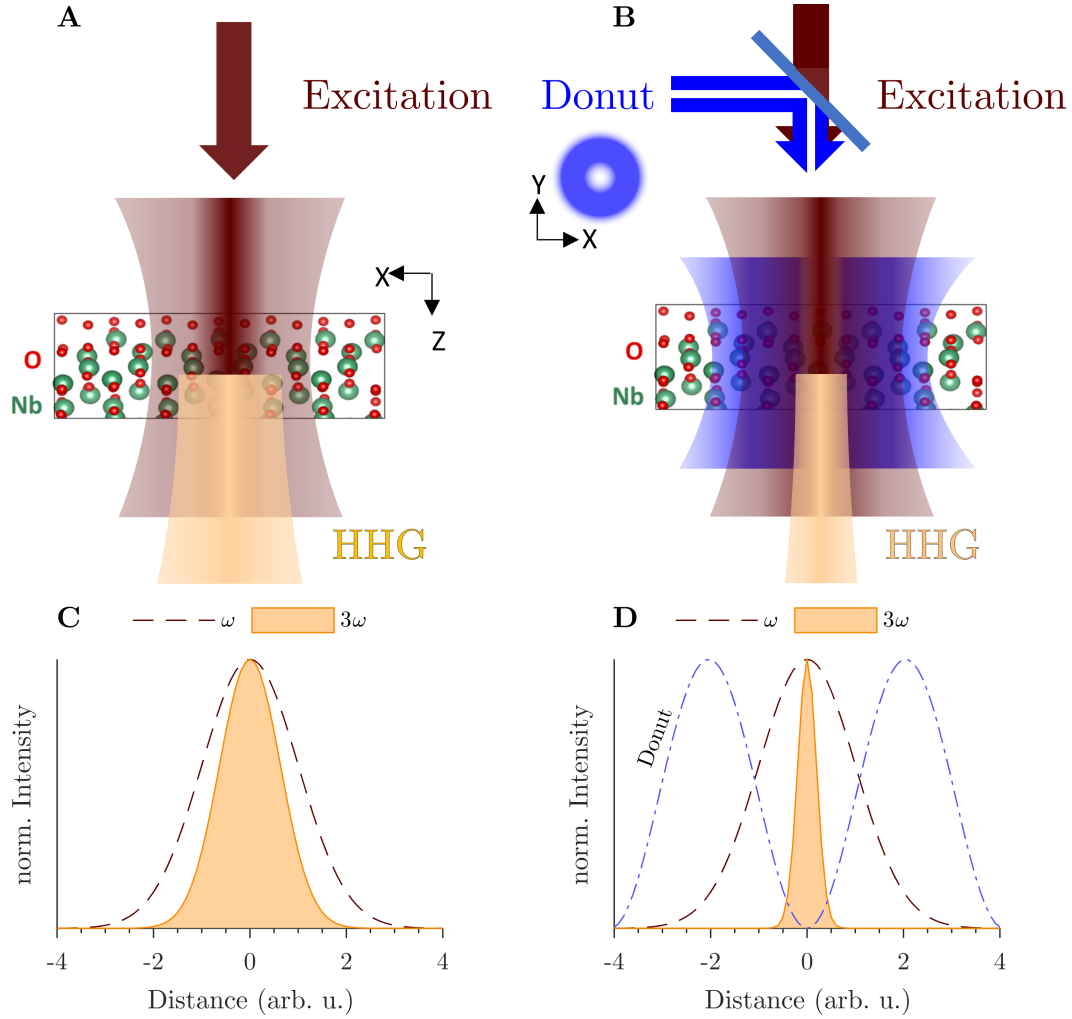


Fig. 1. Principle of HADES. Schematic of the illumination scheme (a,c) and normalized intensities in the focal spot (b,d) for high harmonic generation (HHG) microscopy (a,c) and for harmonic deactivation microscopy (HADES)(b,d). In an HHG microscope, a fundamental laser pulse at central frequency ω excites HHG. Compared to this an additional donut-shaped pulse deactivates high harmonic emission outside of the center. The resulting spot size which effectively can be observed is reduced substantially.

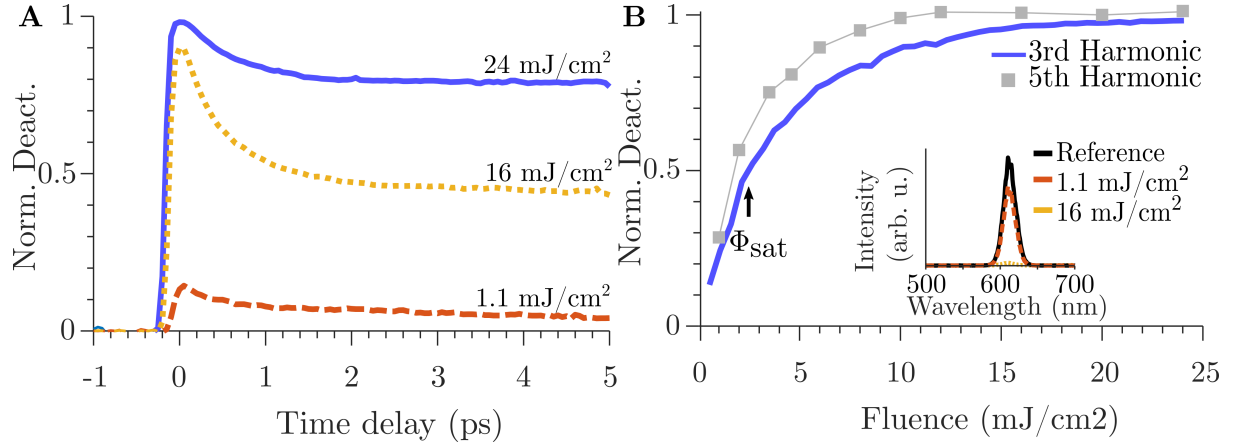


Fig. 2. Deactivation mechanism. a) Time-dependent normalized deactivation of the third harmonic response plotted at rising fluences of the modulation pulse. At negative times the NIR excitation pulse arrives first. The strongest deactivation is always seen at the temporal overlap of the two pulses. b) Fluence-dependent deactivation of the third harmonic (blue) and fifth harmonic (grey, taken from (41)) normalized to the reference harmonic emission without modulation pulse. The saturation fluence ϕ_{sat} is defined as the point of 50 % normalized deactivation. The fifth harmonic shows steeper deactivation and potentially better resolution improvement. The inset shows the third harmonic spectra of the reference (blue) and the spectra with a modulation fluence of 1 mJ/cm² (orange) and a modulation fluence of 16 mJ/cm² (yellow).

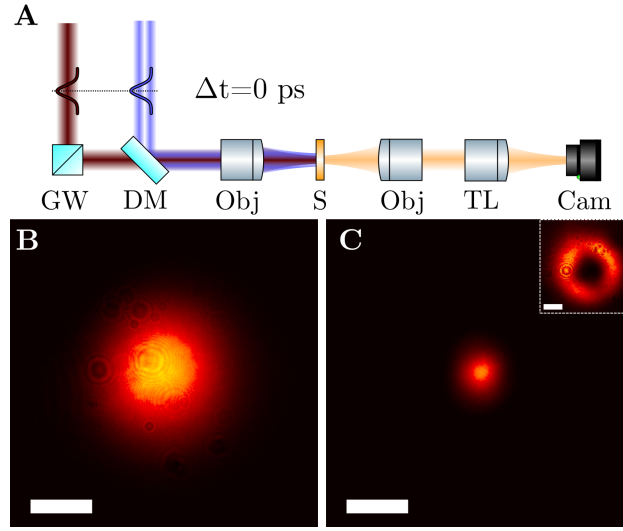


Fig. 3. Point-spread function reduction with donut pulse. The excitation pulse (red) and donut pulse (blue) get combined and focused onto the sample by a lens with a 30 cm focal length. A home-built microscope images the point-spread function (PSF) of the transmitted harmonics (a). PSF on the sample without (b) and with (c) the OAM pulse, the inset shows the deactivation pulse. The bar is 30 μm , which is the resolution limit of the focusing objective at the THG wavelength. GW, glass wedge; DM, dichroic mirror; Obj, Objective lens; S, sample; TL, tube lens; Cam, camera.

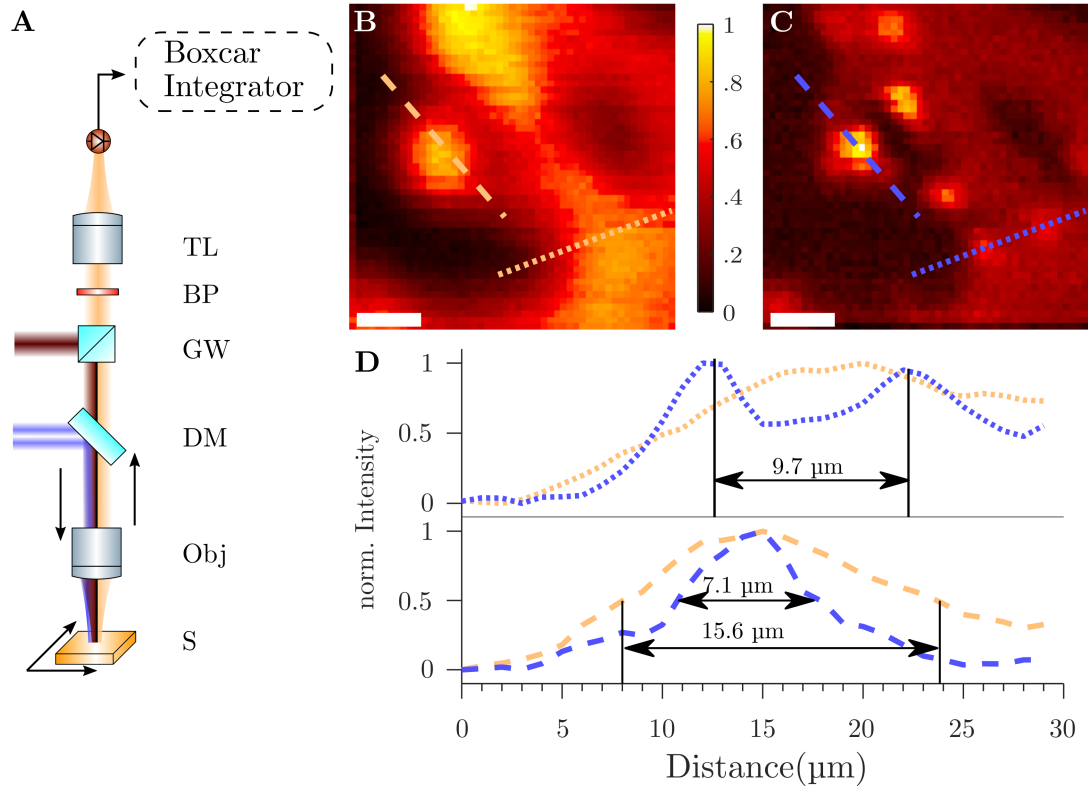


Fig. 4. Resolution improvement through HADES. An NIR (red) and NIR donut-shaped (blue) pulse are focused onto the sample (a). The back-reflected third-harmonics (orange) are detected by an APD. Scanning the sample through the focus spot generates the image. Blocking the donut pulse results in a third-harmonic generation (THG) image (b). Adding the donut pulse (c) gives rise to an image through harmonic deactivation microscopy (HADES). The color bar applies to both images and shows the normalized intensity. The scale bar is 10 μm . The lower panel (d) shows profiles along the dotted line and the dashed line in the above pictures. The profiles in blue are taken from the THG microscopy picture and in orange from the HADES picture. These profiles show a notable resolution improvement for HADES over THG microscopy. GW, glass wedge; DM, dichroic mirror; Obj, objective lens; S, sample; TL, tube lens; BP, bandpass filter; APD, avalanche photodiode.

Supplementary Materials for

Breaking Abbe's diffraction limit with harmonic deactivation microscopy

Kevin Murzyn et al.

*Corresponding author. Email: k.murzyn@arcnl.nl, p.kraus@arcnl.nl

This PDF file includes:

Supplementary Text
Figs. S1 to S5

Supplementary Text

Experiments

The experimental setup is a modified Mach-Zehnder interferometer (Fig. S1). The arm in the vertical direction is the generating arm and in the horizontal direction is the arm of the deactivation pulses. In the generating arm, an optical parametric amplifier (OPA) converts the wavelength of the fundamental pulse from 800 nm to 1800 nm (NIR pulse). In the deactivation arm, a vortex phase plate is inserted to generate the donut pulse. Three different ways enable the detection of emitted harmonics. A wide field microscope images the point-spread function (PSF). A UV/Vis spectrometer resolves the spectrum in reflection. An avalanche photodiode detects individual pulses for raster scanning imaging.

Resolution limit of HADES

The formula for the resolution limit starts at Abbe's diffraction limit for the NIR excitation laser with wavelength λ_0 :

$$d_0 = \frac{\lambda_0}{2 * NA}. \quad (S 1)$$

Where the d_0 is the minimum distance of two point sources. For focusing a laser pulse the effective NA can be calculated as:

$$NA = \frac{\pi * w_0}{4 * f}, \quad (S 2)$$

With the pulse waist w_0 of the collimated pulse and the focus length f of the lens. We assume perturbative non-linear optics therefore the initial Gaussian-shaped pulse intensity of the n -th harmonic can be described as:

$$I_{nth-HG}(x, y) \sim I_{NIR}^n(x, y) = \exp\left(-\frac{x^2 + y^2}{(d_0/\sqrt{n})^2}\right), \quad (S 3)$$

Extracting the pulse waist leads to the resolution of the n -th harmonic as:

$$d = \frac{\lambda_0}{2 * NA * \sqrt{n}}. \quad (S 4)$$

The introduction of the resolution is based on the phenomenological observation that in the simulation the improvement will increase if the peak fluence increases. Therefore, we adapt the formula in (46) to be:

$$d_{HADES} = \frac{\lambda_0}{2 * NA * \sqrt{n}} * \frac{1}{\sqrt{1 + \zeta}}, \quad (S 5)$$

with the saturation level ζ .

PSF Model for one and two-dimension

Two models are introduced for estimating the point-spread function (PSF) reduction in one and two dimensions (Fig. S2, S3). For one dimension a Gaussian PSF of the NIR excitation pulse was assumed which then translates to a Gaussian distribution of the THG as shown above. We approximated the intensity profile of the one-dimensional donut beam with a \cos^2 function. The experimental results of the deactivation from Fig. 2 are then interpolated into the donut profile.

Multiplying the deactivation profile with the Gaussian distribution leads to a narrower PSF. For the two-dimensional case, the experimental observed donut intensity distribution was used to interpolate the deactivation profile. The uneven surface of the sample leads to an underestimation of the achievable PSF.

Convolution of HADES

The images obtained by HADES were convolved with a 2D Gaussian distribution Fig. S4. The Gaussian distribution had to be made asymmetric and rotated. To minimize edge effect the convolution was carried out in accordance with the convolution theorem. The following formula was used for the Gaussian distribution in the frequency space:

$$f(x,y) = \frac{1}{2\pi\sigma_x\sigma_y} \exp(-(ax^2 + bxy + cy^2)), \quad (\text{S } 6)$$

with

$$a = \frac{\cos^2(\theta)}{2\sigma_x} + \frac{\sin^2(\theta)}{2\sigma_y}, \quad (\text{S } 7)$$

$$b = -\frac{\sin(2\theta)}{4\sigma_x} + \frac{\sin(2\theta)}{4\sigma_y}, \quad (\text{S } 8)$$

$$c = \frac{\sin^2(\theta)}{2\sigma_x} + \frac{\cos^2(\theta)}{2\sigma_y}. \quad (\text{S } 9)$$

The parameters to obtain the resulting convolution are $\sigma_x = 0.08 \mu\text{m}^{-1}$, $\sigma_y = 0.13 \mu\text{m}^{-1}$ and $\theta = 45^\circ$. The multiplication of the Fourier transformed picture with the Gaussian was inverse Fourier transformed to get the convolution. As harmonic generation is generally a coherent process, in principle any convolution needs to take into account the phase of the emitted light. We cannot access the phase in our current experiments. However, the sample we are looking at is mostly governed by amplitude variations, consisting of regions with sample (bright emission) and no sample (no emission). Therefore, assuming a flat phase, which is equivalent to an intensity cross correlation as performed above, is a fair assumption.

Fourier ring correlation

To quantify the resolution improvement, we use the single image Fourier ring correlation (FRC) algorithm by [57] on the images in Fig 4b) and 4c). The Fourier transform of each image was masked at the axis to suppress scanning artifacts (Fig. S5a,b). The colorbars in these images are shown on a logarithmic scale. For the single image FRC (Fig. S5c), the pixels get subdivided into two pairs of subimages. A FRC is performed, and the resolution is determined at the 1/7 threshold. The reduced range in frequency space is explained by this subdivision a recalibration is needed as descirebed in [57].

Light microscopy images

The bright-field microscopy (Fig. S6a) images were taken with an effective magnification of 80. The dark-field microscopy images were taken with an effective magnification of 50. The position was traced back through the absolute coordinates of the stage in the Mach-Zehnder interferometer in combination with markers on the sample. The Darkfield microscopy (Fig. S6b) images show a roughening of the surface of the sample.

Electron Microscopy images

In the electron microscopy images (Fig. S7), the nanostructure from the laser damage becomes visible. This nanostructure enhances the third harmonic generation of the thin film. The deep “L” shaped trench shows a complete ablation of the NbO₂ film.

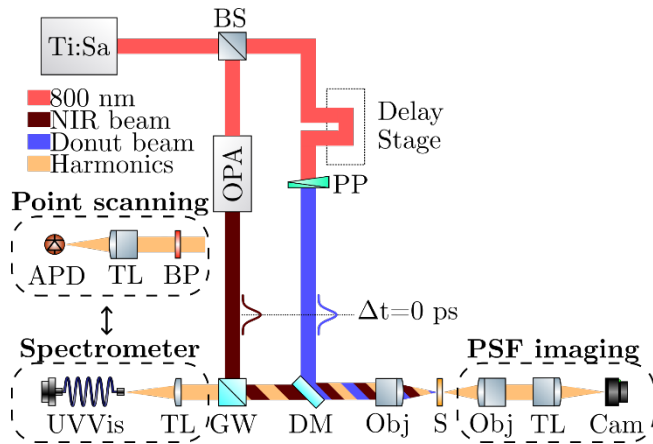


Fig. S1. Experimental setup

The experimental setup is a modified Mach-Zehnder interferometer. In the generating arm, an optical parametric amplifier (OPA) converts the wavelength of the fundamental beam from 800 nm to 1800 nm (NIR beam). In the deactivation arm, a spiral phase plate is inserted to generate the donut beam. Three different ways enable the detection of emitted harmonics. A wide field microscope images the point-spread function (PSF). A UV/Vis spectrometer resolves the spectrum in reflection. An avalanche photodiode detects individual pulses for raster scanning imaging. For more details refer to the main text. BS, beam splitter; OPA, optical parametric amplifier; PP, spiral phase plate; GW, glass wedge; DM, dichroic mirror; Obj, objective lens; S, sample; TL, tube lens; Cam, camera; BP, bandpass filter; UVVis, Fiber spectrometer; APD, avalanche photodiode.

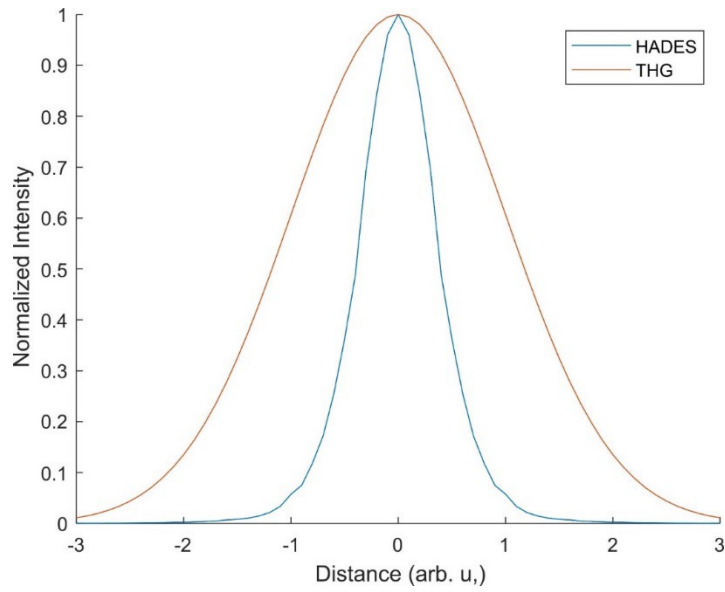


Fig. S2. One-dimensional model of point-spread function

Assumed Gaussian intensity distribution for third harmonic generation (orange). This is combined with a deactivation profile which is assumed to be of the form $\cos^2(x)$, where x is the distance. The deactivation is taken from the normalized deactivation in Fig. 2 of the main text. The peak fluence is assumed to be 25 mJ/cm². The resulting Gaussian peak of the harmonic deactivation microscopy (HADES) is smaller by a factor of three.

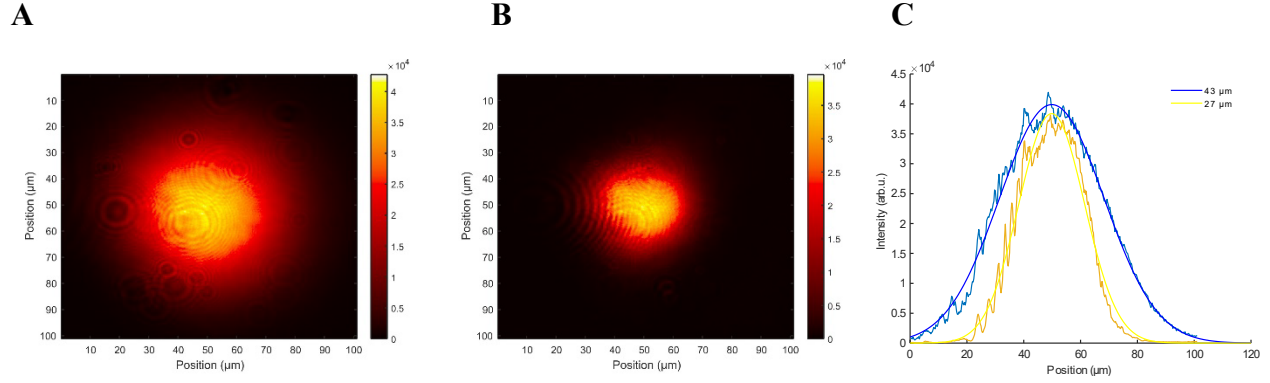


Fig. S3. Two-dimensional model

Two-dimensional (2D) model of the deactivation PSF based on experimental data. The original PSF of the third harmonic (a) gets deactivated by the donut beam (inset Fig. 3c). Assuming a peak fluence of 25 mJ/cm² the resulting PSF is shown (b). Lineouts of the PSF are shown in c) with the FWHM of the 1D fits of THG and HADES respectively. The 2D model shows an underestimation of the experimentally reached deactivation. This can partially be backtracked to the diffraction pattern from the imaging path of the donut beam. These diffraction patterns lead to a wrong estimation of the peak fluence position, and therefore an underestimation of the fluence profile.

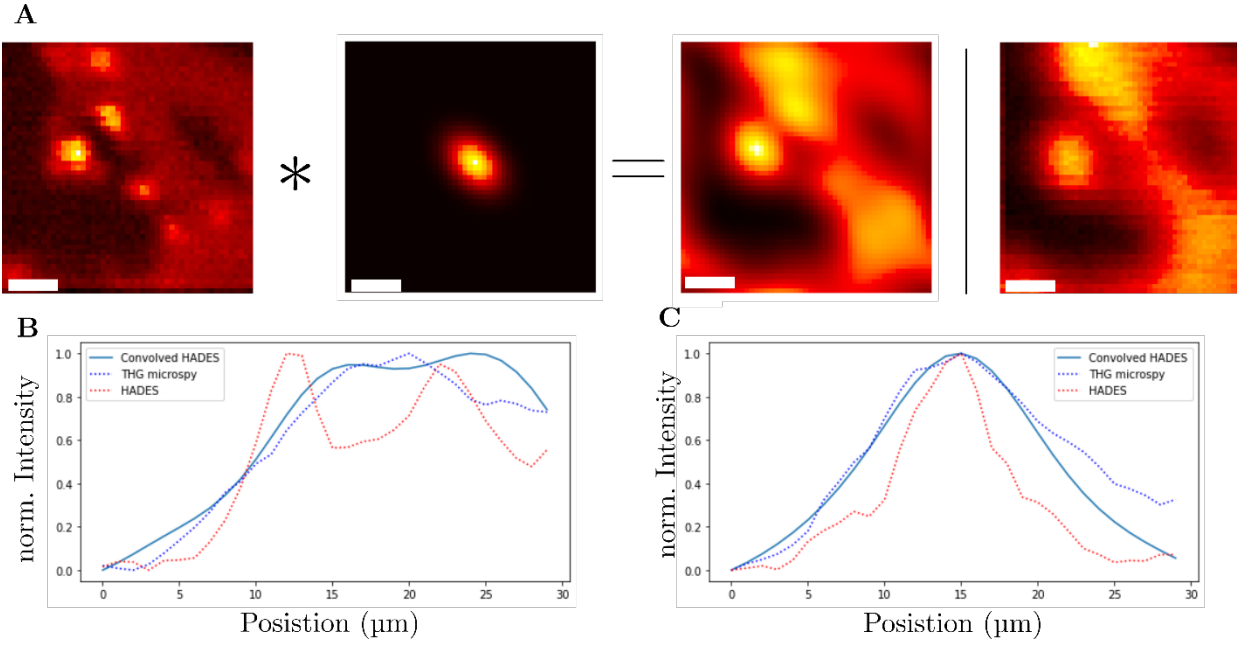


Fig. S4. Convolutions of HADES images

a) The whole image taken by HADES is convolved with an asymmetric and rotated Gaussian distribution. The resulting image resembles the image taken by third-harmonic generation (THG) microscopy (far right). b) Dotted profile as shown in Fig. 4. of the main text. The solid line shows a convolution of the HADES profile with a Gaussian. Only on the edges of the profile lines does the convolution show bigger differences to the THG profile. c) Dashed profile as shown in Fig. 4 in the main text. The solid line shows the convolution of the HADES profile. At the right edge, the convolved lineout shows a larger difference to the THG profile due to the missing 2D information, which contains a blurred edge in the THG image but not in the HADES image.

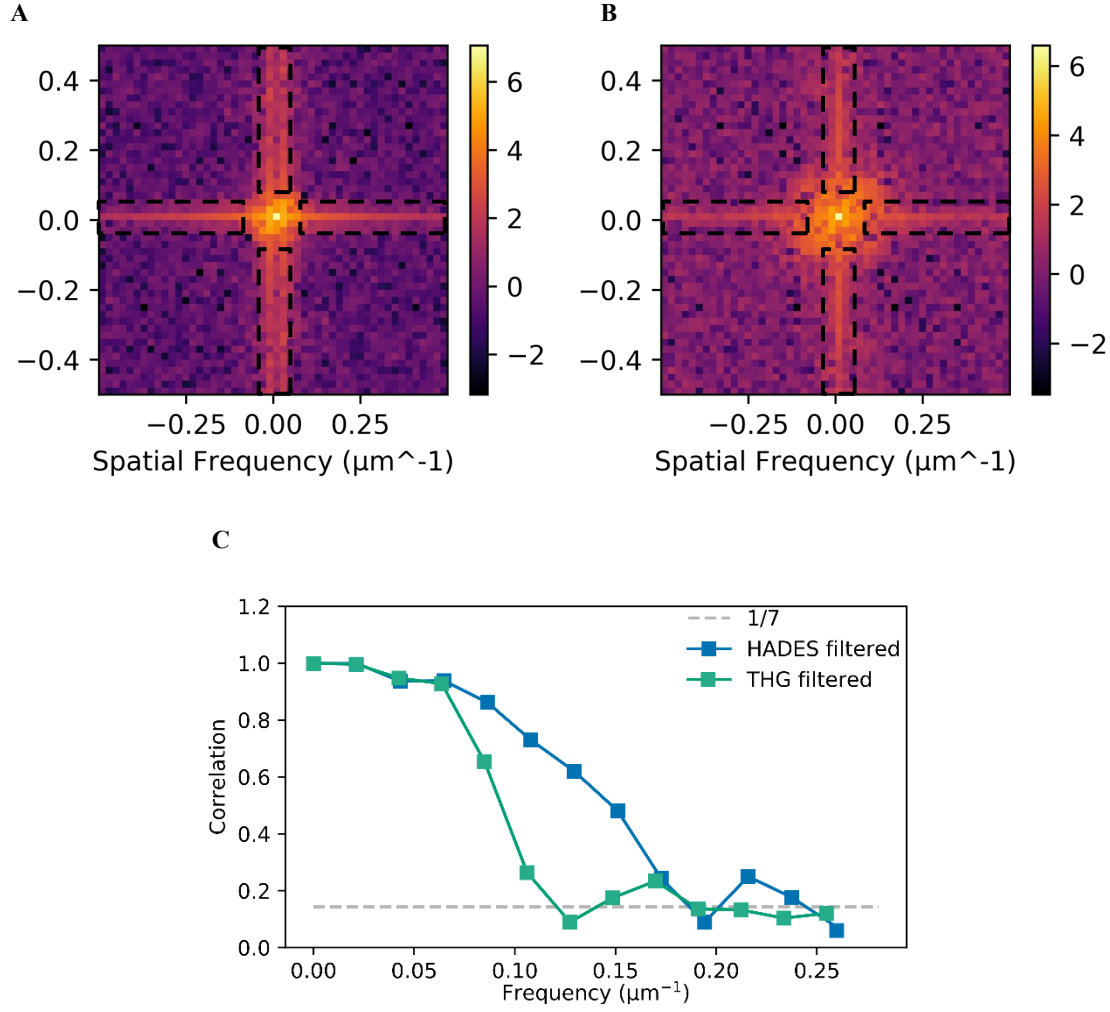


Fig. S5. Fourier ring correlation

Fourier transforms of A) the THG image and B) the HADES image shown in Fig. 4B and Fig. 4C with logarithmic colorbar. For the one-image Fourier ring correlation (FRC) introduced in [57] to work the artifacts along the axis were masked (black boxes). C) Result of the one image FRC showing a higher correlation for HADES at larger spatial frequencies and a later crossing of the $1/7$ -threshold.

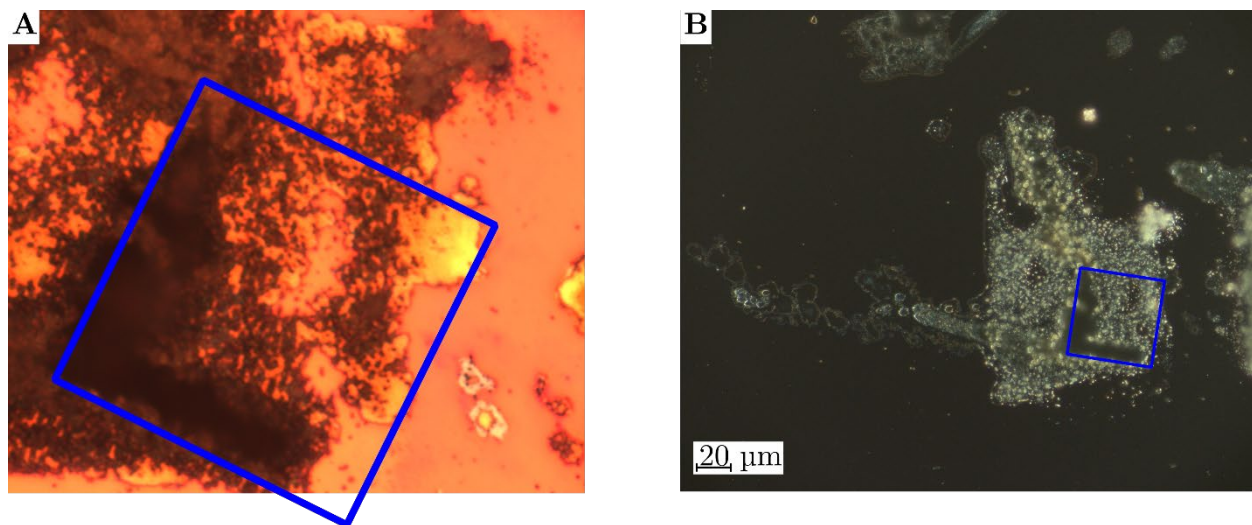


Fig. S6. Full-field microscopy images

Bright-field (a) and dark-field (b) microscopy images of the area images in Fig 4. In the dark field an increased surface roughness of the image can be seen. This indicates the thermal damage of the thin film. The “L”-shaped area is a complete ablation of the thin film.

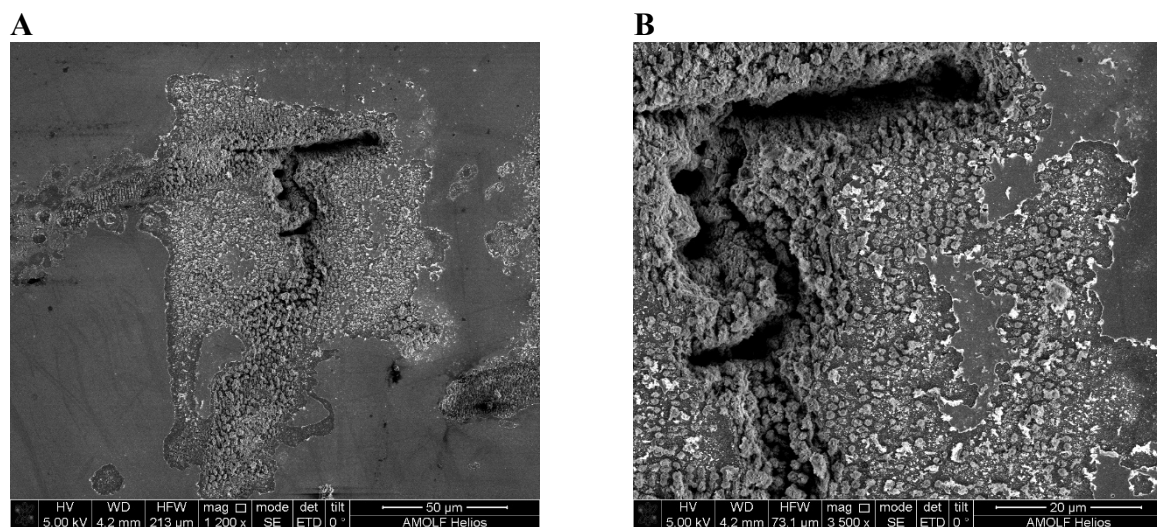


Fig. S7. Scanning electron microscopy images

a) Overview of the scanned area that got imaged with THG and HADES. Compared to the scanning and full-field images these images are flipped along the horizontal axis. b) Zoomed-in version of the scanned images shown before. The nanostructures on the surface are visible. It can be the reason for the enhancement of the THG at certain positions.